

## Modeling of a soft clay gentle slope with sand layer in centrifuge under seismic loading: PIV and strain rate analysis

Lucas Chinem Takayassu<sup>1#</sup> , Cristian Yair Soriano Camelo<sup>2</sup> ,  
Marcio de Souza Soares de Almeida<sup>1</sup> , Maria Cascão Ferreira de Almeida<sup>3</sup> ,  
Santana Phani Gopal Madabhushi<sup>4</sup> , Ricardo Garske Borges<sup>5</sup> 

Article

### Keywords

Centrifuge modeling  
PIV  
Gentle slopes  
Layered profile  
Seismic response  
Strain rate effect

### Abstract

Dynamic soil parameters such as the shear modulus suffer degradation while damping in soil increases under dynamic loading. These can be determined from various tests such as element tests, field tests and centrifuge experiments. Most of the studies about dynamic soil characterization have focused on evaluating these parameters assuming horizontal ground conditions without considering the effect of static shear stresses induced by ground inclination. This paper presents a dynamic centrifuge test conducted on a layered gentle slope comprising clay and sand, to obtain experimental data in terms of shear modulus and damping for various shear strains. Particle Image Velocimetry (PIV) was employed to measure the displacements and to calculate accelerations due to seismic loading at various depths throughout the slope model. The results suggest that the static shear stress caused by the profile inclination causes a more pronounced degradation of the shear modulus when compared to flat ground conditions. Moreover, the damping during the centrifuge test exhibited larger values than expected, following a similar behavior observed in other experimental programs. The strain rate analysis revealed the mobilization of shear stresses higher than the monotonic shear strength for the clay layers during the seismic shaking.

## 1. Introduction

Evaluation of dynamic soil parameters is essential to understand how sites will respond during an earthquake event. To simulate the dynamic response of soil sites, numerical models employ shear modulus degradation and damping variation curves. Families of curves have been developed for different materials based on element tests (Kokusho, 1980; Vucetic & Dobry, 1991; Darendeli, 2001; Vucetic & Mortezaie, 2015), field investigations (Chang et al., 1989; Zeghal et al., 1995; Yang et al., 2017).

Most of the reported literature on dynamic centrifuge testing employed for the estimation of stiffness and damping parameters has considered horizontal or level ground profiles in sand, clay and a combination of both (Elgamal et al., 1996; Brennan et al., 2005; Rayhani & El Naggar, 2007; Li et al., 2013). However, there are few reported data on the evaluation of the stiffness and damping for canyons (Tarazona et al.,

2019) and sloping grounds (Soriano Camelo et al., 2022). In particular with small inclinations ranging between 1° to 5° (Masson et al., 2006), which are characteristic of continental slopes. As those slopes are under static shear stresses due to ground inclination, this effect has not been addressed before in the measurement of the shear modulus and damping in clay and sandy soils.

Additionally, in centrifuge modeling, small-scale models are subjected to increasing acceleration levels to match a particular prototype stress level. Since the physical centrifuge models are smaller than the prototype by a scale factor,  $N$ , events like earthquakes will occur more rapidly in the model than in the prototype (Sathialingam & Kutter, 1989). In dynamic centrifuge testing, during the simulation of earthquakes, the time is scaled by a factor equal to  $N$ . This means that the rate of change of stresses and strains occurs  $N$ -times faster in the model than in the prototype. The dynamic response of soils is closely related to the rate

<sup>#</sup>Corresponding author. E-mail address: lucas.takayassu@coc.ufrj.br

<sup>1</sup>Universidade Federal do Rio de Janeiro, Instituto Alberto Luiz Coimbra, Rio de Janeiro, RJ, Brasil.

<sup>2</sup>Université Gustave Eiffel, CG-lab, Nantes, France.

<sup>3</sup>Universidade Federal do Rio de Janeiro, Escola Politécnica, Rio de Janeiro, RJ, Brasil.

<sup>4</sup>University of Cambridge, Cambridge, United Kingdom.

<sup>5</sup>Petrobras, Centro de Pesquisa e Desenvolvimento, Rio de Janeiro, RJ, Brasil.

Submitted on April 5, 2023; Final Acceptance on October 25, 2023; Discussion open until February 28, 2024.

<https://doi.org/10.28927/SR.2023.003223>



This is an Open Access article distributed under the terms of the Creative Commons Attribution License, which permits unrestricted use, distribution, and reproduction in any medium, provided the original work is properly cited.

of strain, and can be studied by analyzing experimental data obtained from centrifuge tests. Specifically, the displacements and accelerations observed during these tests can provide valuable insights into the effect of strain rate on soil behavior.

This paper aims to evaluate the shear modulus and damping variation of clay in an inclined ground profile or gentle slope. To achieve this, a centrifuge test was carried out in a layered soil profile consisting on a sand layer between two soft clay layers. Stress-strain data was measured to obtain modulus and damping data points at various level of shear strains by measurements of accelerations and displacements by means of Particle Image Velocimetry (PIV) at various locations in the slope. The PIV measurements were validated on the basis of recorded data of accelerometers and displacement transducers also installed in the slope model. A set of earthquakes with varying amplitudes and frequency content were applied to the model using a shaking table. Typically, in centrifuge experiments, a dense array of accelerometers is employed. However, this arrangement can interfere in the soil response if the soil layer is too thin. Moreover, an accelerometer malfunction could interfere with the calculation of dynamic soil parameters when using the methodology of downhole arrays. The PIV methodology can overcome such constraints as it employs a non-intrusive methodology, providing complementary data with a greater number of normalized shear modulus points. At the end, a strain rate analysis evaluates its effect on shear strength.

## 2. Materials and methods

A layered gentle slope model, with an inclination of three degrees, was tested at an acceleration level of 60-g on the 10 m diameter beam centrifuge at the Schofield Centre, University of Cambridge (Schofield, 1980; Madabhushi, 2014). The slope model was built inside a laminar box and

then subjected to a set of earthquakes by means of a shaking table driven by a servo hydraulic actuator (Madabhushi et al., 2012).

### 2.1 Materials and model preparation

Three soil layers compose the model profile: two clay layers and an intermediate Hostun sand layer, as shown in Figure 1. For the clay layers, Speswhite kaolin was employed (Almeida, 1984, Vardanega et al., 2012), with the following properties (Lau, 2015): liquid limit,  $LL = 63\%$ ; plastic limit,  $PL = 30\%$ ; plasticity index  $PI = 33\%$ ; and specific gravity,  $G_s = 2.60$ . The intermediate soil layer was composed of Hostun Sand (Colliat et al., 1986; Chian et al., 2014). For the present study, the values adopted were (Azeiteiro et al., 2017): critical state friction angle,  $\phi_{crit} = 31.5^\circ$ ; specific gravity,  $G_s = 2.64$ ; minimum void ratio,  $e_{min} = 0.66$ ; maximum void ratio,  $e_{max} = 1.00$ .

The clay was mixed with water, under vacuum, with a water content ( $w$ ) of around 120%. This material was placed in a consolidation box (500 mm length x 250 mm height) and a consolidation pressure of 250 kPa was applied (Soriano Camelo et al., 2021). After two weeks under constant final stress the clay block was removed from the box and cut horizontally in two parts: the lower layer with 150 mm and the upper layer with 80-90 mm. The sand layer was prepared in two plastic boxes measuring 250 x 250 x 50mm. The containers were filled with deaired water. With the help of an adapted nozzle and a controlled drop height, a relative density (RD) of 45% (void ratio,  $e = 0.85$ ) was achieved. The sand blocks were then stored in freezers for 24 hours to obtain a solid material to enable manipulation and positioning of the sand layer over a lower clay layer and subsequent placement of the top clay layer. This resulted in a three-layer block which was covered by a rubber bag to

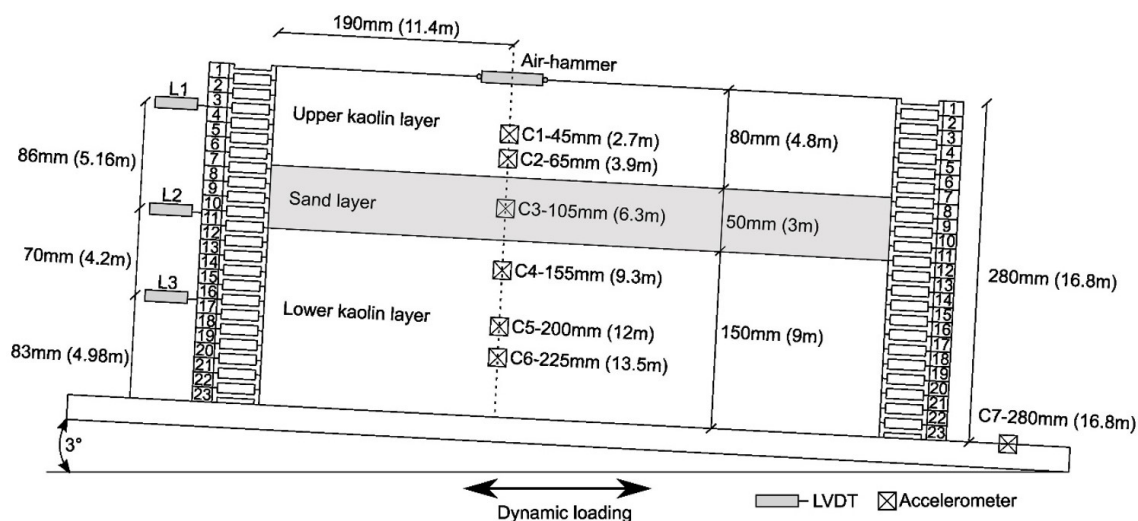


**Figure 1.** Centrifuge instrumented model, column (C1-C6) and base (C7) accelerometers with respective depths in millimeters. Model scale, prototype scale in parentheses.

avoid the leakage of water. In the sequence, the frames of the laminar container were installed one-by-one across the layered block until reaching the final height of the model (Soriano Camelo et al., 2021). The final soil profile is presented in Figure 1, composed of a superficial layer of clay with a thickness of 80 mm, a central 50 mm sand layer and finally the lower clay layer with a thickness of 150 mm.

After the preparation of the layered profile, the model was instrumented with seven piezoelectric accelerometers (C1 to C7 in Figure 1), three linear variable differential transformers (LVDTs, L1 to L3 in Figure 1) and an air hammer placed at the surface of the model to obtain shear wave velocity data points. For the PIV analysis, a set of markers were glued to each lamina of the model container, and a high-speed camera was placed in front of the model (Soriano Camelo et al., 2021).

## 2.2 Particle Image Velocimetry setup

Particle Image Velocimetry (PIV) technique was used in the centrifuge test during the earthquake loading. A high-speed camera (MotionBLITZ EoSens mini2 by Mikrotron GmbH) was employed to monitor the dynamic response of the model (Soriano Camelo et al., 2021). The images were recorded at a resolution of 1504 x 1050 pixels with an acquisition rate of 953 Hz. A total of 1354 frames were defined for each earthquake to capture the condition of the model before, during and after the application of the shaking. An external trigger started the camera, and it was set to generate footage with 15% of the frames recorded before the earthquake and the remaining frames to record the seismic shakings applied to the model.

To capture the movements of the soil/laminar box system, circular fiducial markers were used for PIV analysis. The placement of the markers is shown in Figure 2 and are

referred to in this study by the letter “M” followed by the number of the layer to which they were attached. The markers identified as Fixed 1 and Fixed 2 were employed to track the displacements associated with the input motion at the base of the model. Those markers were attached to a column fixed to the base of the model container. Due to space restrictions, the camera field of view covered only markers M3 to M17 and markers Fixed 1 and Fixed 2 as shown in Figure 2. The recorded photos were scaled from pixel dimensions to distance dimensions using a checkerboard sheet with a 20 mm x 20 mm pattern.

The XnConvert editing tool was used for batch processing of the images for the PIV analysis. Several adjustments were made to improve the contrast of the photo sequence. The marker displacements were tracked using an open-source software (Blender - Hess, 2010), employed for modeling, animation and video editing in 2D and 3D. The tracking routine was configured for “Location Only” motion capture function with a default correlation factor of 0.75.

## 2.3 Centrifuge test

The centrifuge was accelerated in increments of 10-g until reaching a level of 60-g. Afterwards, the model was kept in flight for around 1 hour for pore pressure equilibrium. Subsequently, a set of earthquakes of varying frequency content and amplitudes were applied to the model. Table 1 and Figure 3 present the characteristics and time histories of the applied ground motions. The earthquakes consisted of three sinusoidal (1 Hz) waves and one real scaled motion (Kobe, 1 Hz-4 Hz), this earthquake have been widely studied in literature (Lu & Hwang, 2019; Sahoo & Shukla, 2021) with Peak Ground Accelerations (PGA) varying between 0.06 g and 0.29 g and Significant Durations ( $D_{595}$ ) varying between 4.69 s and 9.59 s.

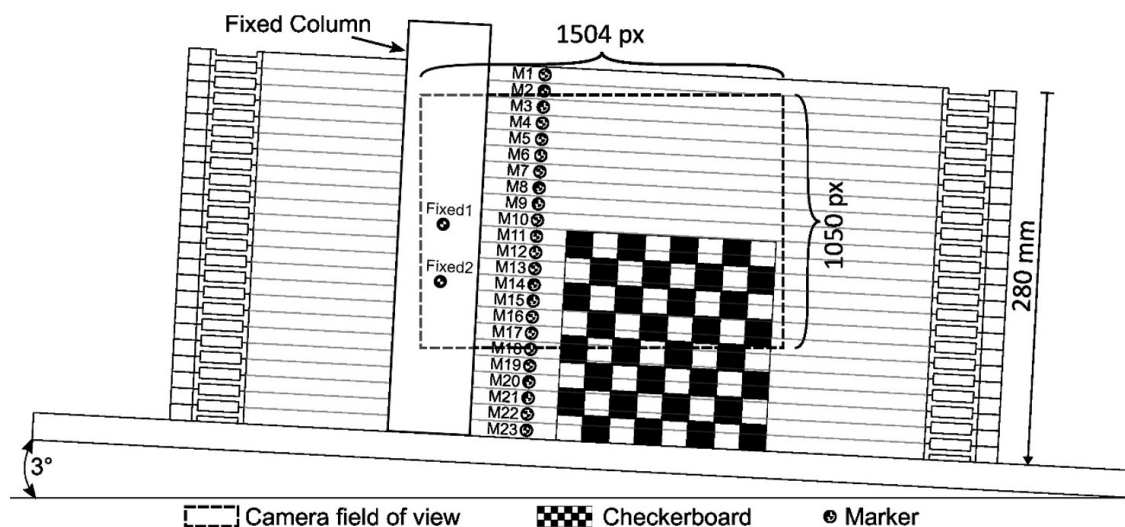


**Figure 2.** Position of the circular fiducial markers used for the PIV, camera field of view area and checkerboard sheet pattern.

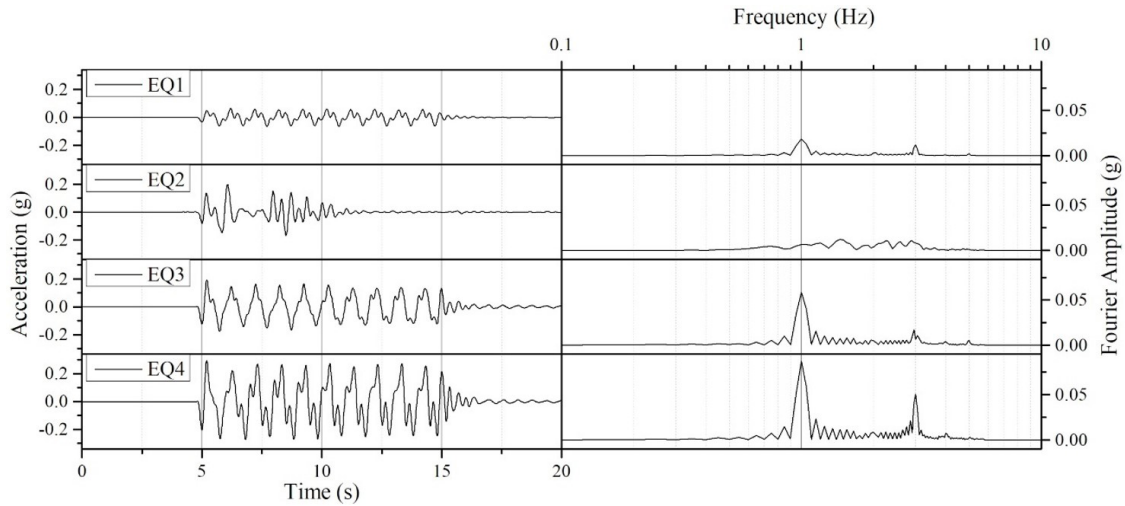


**Figure 3.** Ground motions at the base of the model: measured acceleration-time histories and Fourier amplitude (prototype scale).

**Table 1.** Input motions recorded at the base of the model, prototype scale.

Code	Input	PGA <sub>Base</sub> [g]	$D_{595}$ [s]	Frequency [Hz]
EQ1	Sinusoidal	0.06	9.05	1
EQ2	Kobe	0.2	4.69	1-4
EQ3	Sinusoidal	0.19	9.53	1
EQ4	Sinusoidal	0.29	9.59	1

## 2.4 In-flight characterization tests

In-flight characterization tests were carried out to obtain undrained shear strength and shear wave velocity profiles. Shear wave velocity data points were obtained by means of air hammer tests (Ghosh & Madabhushi, 2002). Arrival times of shear waves generated by the air hammer placed at the surface of the model were measured by the accelerometers placed in the central column of the model (Figure 1). The shear wave velocity data points at the middle depth between accelerometers were estimated based on the distance between the accelerometer and the arrival times (Figure 4a).

The central column of accelerometers (C1 to C6 in Figure 1) was used for the Air Hammer test (Ghosh & Madabhushi, 2002) to calculate the soil shear wave velocity values  $v_s$  and then the initial shear modulus  $G_0$ , calculated using Equation 1 and soil density ( $\rho$ ), as shown in Figure 4a.

$$G_0 = \rho v_s^2 \quad (1)$$

The theoretical initial shear modulus profile was obtained by the Equation 2 proposed by Hardin & Black (1969):

$$G_0 = Af(e) \left( \frac{p'}{p_r} \right)^m OCR^k \quad (2)$$

where:

$G_0$  – Initial shear modulus [MPa]

$p'$  – Average effective stress [kPa]

$p_r$  – Reference stress (100 kPa)

$OCR$  – Over consolidation ratio

$A, f(e), k$  and  $m$  – Correlated parameters

The constants  $A, f(e), k$  and  $m$  are correlated parameters. The reference values used in this study are shown in Table 2.

The undrained shear strength ( $s_u$ ) profile was obtained from a mini-Cone Penetration Test (CPT), using Equation 3 and a cone factor ( $N_{kt}$ ) equal to 16 (Herrerros, 2020), as shown in Figure 4b. The upper clay layer exhibited  $s_u$  values ranging from 8 to 26 kPa and the deeper clay layer presented an average  $s_u$  of 26 kPa.

$$s_u = \frac{q_c}{N_{kt}} \quad (3)$$

where:

$s_u$  – Undrained shear strength [kPa]

$q_c$  – Measured cone tip resistance [kPa]

Theoretical values of  $s_u$  were estimated using Equation 4 (Wroth, 1984) with the parameters  $K = 0.23$  and  $n = 0.62$  proposed by Zhang et al. (2011) for Speswhite kaolin. The results presented a reasonable agreement with the experimental results for the upper clay layer (Figure 4b).

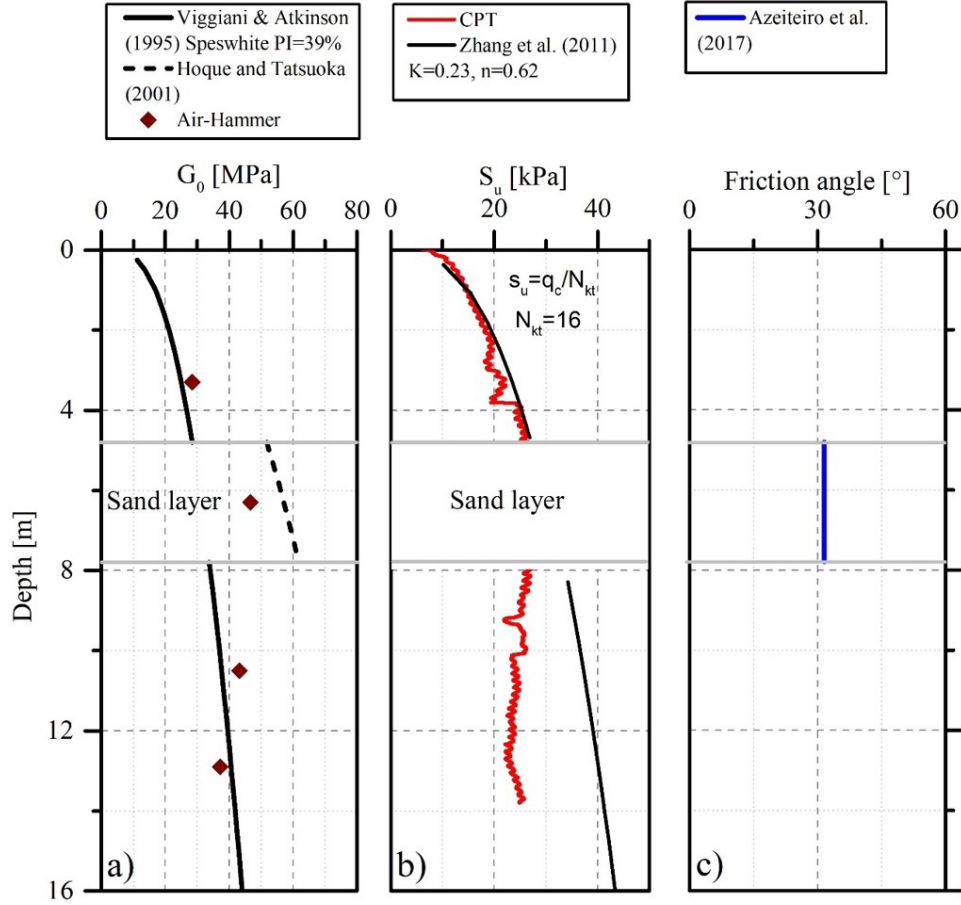


**Figure 4.** (a)  $G_0$  profile and  $G_0$  points generated by “Air-hammer”; (b) Undrained shear strength,  $S_u$ ; (c) Friction angle of sand layer.

**Table 2.** Fitting constant values.

Soil	$A$	$f(e)$	$k$	$m$	Reference
Hostun Sand	80	$\frac{(2.17 - e)^2}{1 + e}$	0	0.47	Hoque & Tatsuoka (2000)
Speswhite Kaolin	750	1	0.25	0.83	Viggiani & Atkinson (1995) IP=39%

For the deeper layer, the empirical correlation exhibited higher values when compared with data obtained from the CPT.

$$s_u = K \cdot \sigma_v' (OCR)^n \quad (4)$$

where:

$K$  – Normally consolidated strength ratio

$\sigma_v'$  – Effective vertical stress [kPa]

$OCR$  – Overconsolidation ratio

$n$  – Plastic volumetric strain ratio

Figure 4c shows the value of the friction angle of the Hostun sand obtained by a series of triaxial test performed by Azeiteiro et al. (2017) for loose and moderately loose samples.

### 3. Results

By measuring seismic displacements throughout the slope model, the use of the PIV technique in this study aims to enable the generation of the shear modulus degradation and damping evolution curves. Therefore, some results are presented first to illustrate the validation of the PIV analysis. This is followed by a summary of the expected results of the normalized shear modulus for all the applied earthquakes.

#### 3.1 Measured displacements

The displacements ( $u$ ) obtained from the PIV analysis and LVDT readings for the EQ3 loading are compared in Figure 5. The position of each instrument and marker can be

seen in Figure 1 and Figure 2. The superficial displacement transducer L1, in Figure 1, detached from the laminar container at the beginning of the test. Therefore, the results from L2 and L3 were used for comparison. Overall, it was observed a good agreement between the measured displacements measured by the LVDTs and the displacements obtained from PIV analysis.

### 3.2 Acceleration-time history and response spectra data

Acceleration ( $\ddot{u}$ ) time history values were obtained for each layer and show the results for the top (C1) and bottom (C7) accelerometers for the EQ3 loading (Figure 1 and Figure 6). Accelerometer data used a bandpass filter with cutoff frequencies [5-350] Hz, in prototype scale. For the PIV analysis, accelerations were obtained through double derivation of displacements plus a Savitzky–Golay filter, using a third-order polynomial and a window size of 11 points. This filter smooths the signal without distorting its trend.

Figure 6 shows good agreement between the PIV and acceleration data. Within the loading phase, the M4 and M5 markers display adequate similarity with the upper accelerometer (C1) signal, Figure 6a. The result obtained by the Fixed1 marker, presented a good phase correlation with the accelerometer result at the base (C7). The latter presented another frequency component outside the single-frequency sinusoidal load (Figure 6b), this characteristic can be better observed on response spectra results. As far as the response spectra (Kramer, 1996) data is concerned, the accelerometer at the base (Figure 7b) shows a second peak outside the loading period of the model. As presented by Brennan et al. (2005),

dynamic loads applied by actuators in centrifuge tests do not necessarily contain only one frequency. Higher frequency harmonics may exist, not necessarily being signal noise.

### 3.3 Calculation of shear stresses and shear strains

For shear stress ( $\tau$ ) and shear strain ( $\gamma$ ) calculations, groups of three adjacent markers were employed. For each loading and group of markers (Figure 8), shear stress calculations were done by implementing trapezoidal integration with shear strains obtained through a second order approximation (Brennan et al., 2005). For these calculations, the markers were divided into two groups: the first corresponding to the clay layers and the second, corresponding to the sand layer to obtain data points for each type of material. An advantage of using the PIV methodology, with a laminar box, was the larger number of points for obtaining the shear strains and shear stresses in the slope when compared with an analysis only employing the accelerometers installed in the model. For the calculations, six groups of markers were employed in the in the clay layers and two groups in the sand layer.

Figure 9 shows an example of a shear stress versus shear strain plot for the bottom clay layer covered by markers M12, M13 and M14 for input motion EQ3. According to Biscontin & Pestana (2006), in a slope, even with a few degrees, there is a static shear stress ( $\tau_s$ ) applied within the soil in the downslope direction of the model. Elgamal et al. (1996) expresses this steady loading as  $\tau_s = \rho g z \sin(\alpha)$ , with mass density ( $\rho$ ), gravity ( $g$ ), depth ( $z$ ) and slope angle ( $\alpha$ ). During dynamic loading, this shear stress generated a

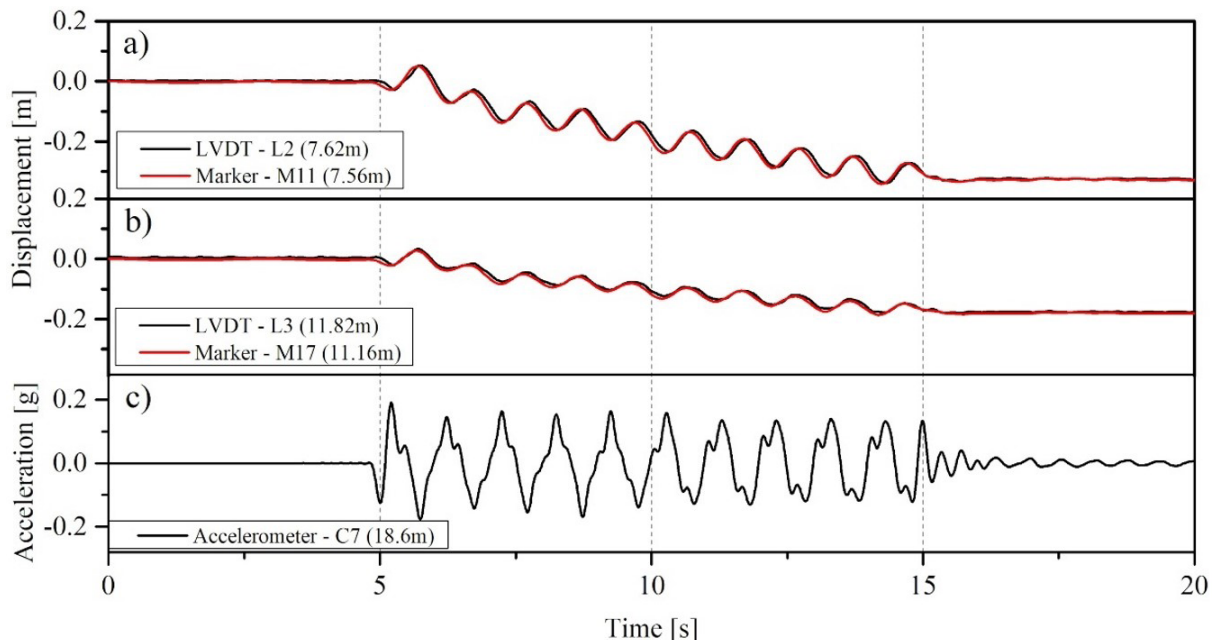


**Figure 5.** Comparison of EQ3 displacements, generated by PIV and LVDTs, values in prototype values: (a) L2 (7.62 m) and M11 (7.56 m); (b) L3 (11.82 m) and M17 (11.16 m); (c) Accelerations at the base of the model (C7).

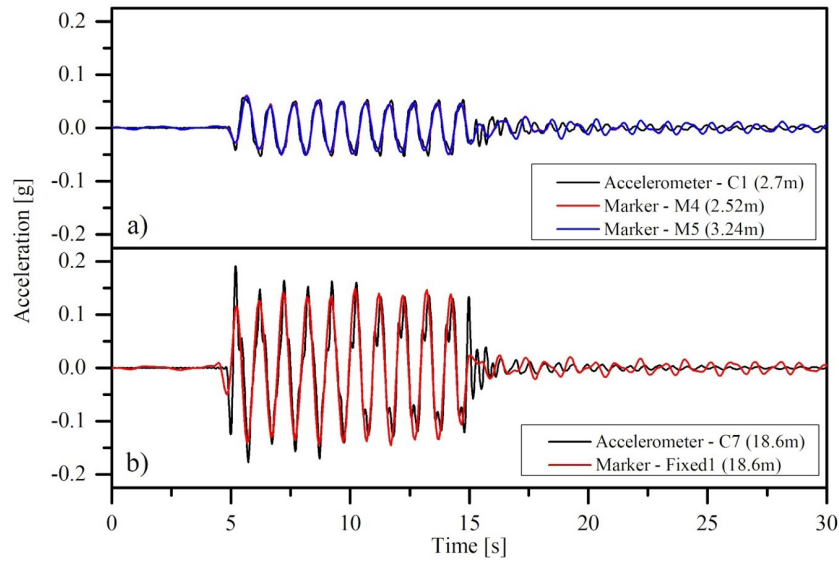


**Figure 6.** Comparison of EQ3 accelerations (prototype scale), between accelerometer and PIV. Depths in parentheses. (a) Top accelerometer (C1) with closest markers (M4 and M5); (b) Base accelerometer (C7) with base marker (Fixed1).

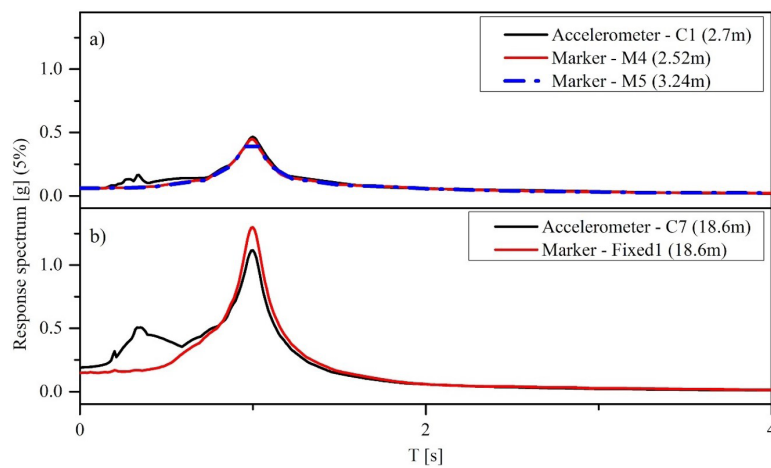


**Figure 7.** Response spectra comparison for EQ3, obtained from accelerometer and PIV: (a) Top accelerometer with closest markers; (b) Base accelerometer with base marker.

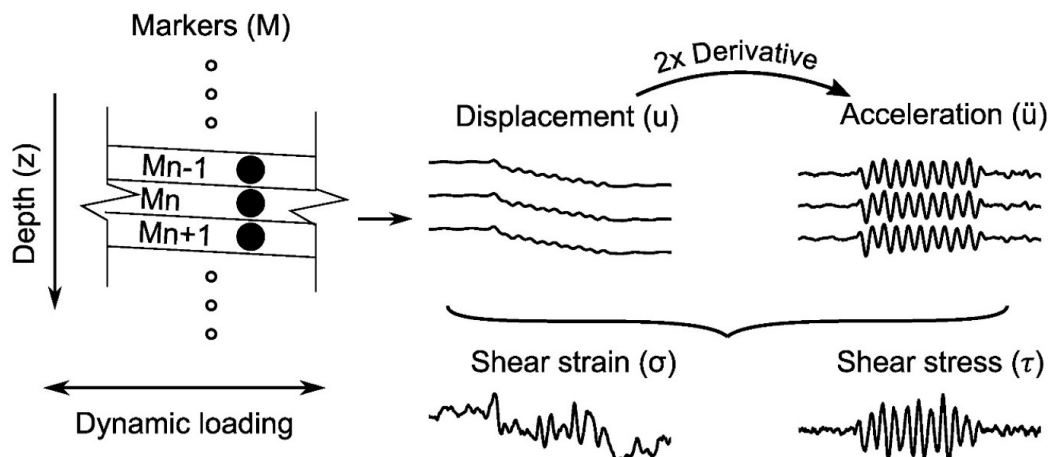


**Figure 8.** Acceleration conversion from PIV displacement.

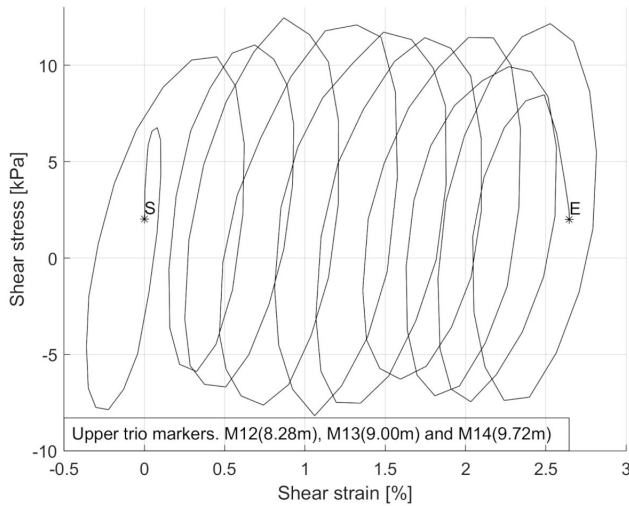


**Figure 9.** Shear stress versus shear strain for loading EQ3 and markers M12, M13 and M14. Prototype depths in parentheses.

shear strain accumulation, caused by the superposition of the static shear stresses with that generated by the dynamic loading, as found by Elgamal et al. (2002). As the signal passes through the soil, a permanent strain can be observed. Strain stress loops starts (S) at around zero strain and a 2.5 kPa static stress. At the end (E) of loading, static stress continues around 2.5 kPa and strain accumulation reaches values above 2.5%.

### 3.3.1 Experimental shear modulus and damping data points

For each applied earthquake, shear stress/strain loops at different depths in the model were obtained. The secant shear modulus was calculated, for each loop, through the tangent line generated by maximum and minimum points. In this way, each trio of markers generates several pairs of secant shear modulus ( $G_{sec}$ ) and shear strain ( $\gamma$ ). Normalized shear modulus ( $G_{norm} = G_{sec} / G_0$ ) at various shear strains was determined using values for  $G_0$  at different depths (Figure 4). The area for each loop was calculated and used to find damping (Afacan et al., 2014).

Figure 10a summarizes the shear modulus values  $G_{norm}$  for the applied input motions. The results are separated according to the type of material (kaolin clay and hostun sand). A distinct behavior was observed between the sand and the clay layers, where the granular material showed a lower shear strain, due to lower degradation in shear resistance during the shaking. The dynamic damping exhibited dispersed values, not indicating a trend, a similar response has been reported in the literature (Tarazona et al., 2019; Afacan et al., 2014; Tsai & Hashash, 2009).

There was a difference in behavior between the upper and lower clay layers (Figure 10b). The deeper layer presented,

on average, a higher normalized shear modulus and strains greater than 1%. The dynamic response of the clay does not depend on the confining stress and the identical material was employed for both clay layers; therefore, normalized shear module ( $G_{norm}$ ) for the upper and lower clay layer should present a similar value. Figure 10b shows the lower layer with values higher than the topmost layer and strains above 1%. One possible explanation for this difference is the increase in the static shear stress with depth, higher static shear stresses may accelerate the shear modulus degradation process. Another probable explanation is the presence of the sand on the wave propagation in the model, acting as a “filter”. To illustrate this, Figure 11 shows the displacement profiles during seismic shaking EQ4 at the location of the PIV markers. Nearly at the beginning of loading (Figure 11a), the markers show no major horizontal displacement. Five seconds later (Figure 11b), there is not a significant variation of values between neighboring points in the sand layer, indicating a probable attenuation of the signal. While the lower clay layer presents greater shear deformations, the upper clay layer and the sand layer present a more rigid behavior. Figure 11c and 11d show similar behavior for the two upper layers, when compared to Figure 11b the increment of strain accumulation in the lower layer is noticeable.

### 3.3.2 Input comparison

Figure 12 presents representative shear modulus reduction curves for clay and sand (Darendeli, 2001) adjusted by means of the GQ/H model (Groholski et al., 2016), compared with the data points obtained from PIV for all input motions analyzed. The centrifugal (experimental) results appear below the reference curves. The empirical curves (Darendeli, 2001) are based on Resonant Column Torsional Shear tests (RCTS), which in turn are unable to evaluate some characteristics present in the centrifuge test under study, such as the slope profile (Soriano Camelo et al., 2021) and heterogeneous layers (Rayhani & El Naggar, 2007). Overall, depending on the type of soil, the range of mobilized shear strains varies. For the sand layer (Figure 12b), the mobilized shear strains reached values up to 0.3% during the application of the earthquakes to the model. Regarding the clay layers, depicted in Figure 12a and Figure 12c, larger shear strains were mobilized with maximum values around 2%. The data points for the sand layer and the clay layers seem to be offset when compared with the reference curves. This has an important implication in the definition of the modulus degradation curves because the effects of the static shear stresses of the sloping ground should be considered, given that there is a more pronounced shear modulus degradation due to the superposition of the dynamic and static shear stresses. All experimental damping, shown in Figure 12, present higher values compared to the reference curves. Strain accumulation favors one direction of movement over the other, for this reason the area enveloped by the shear stress-strain loops employed for the damping

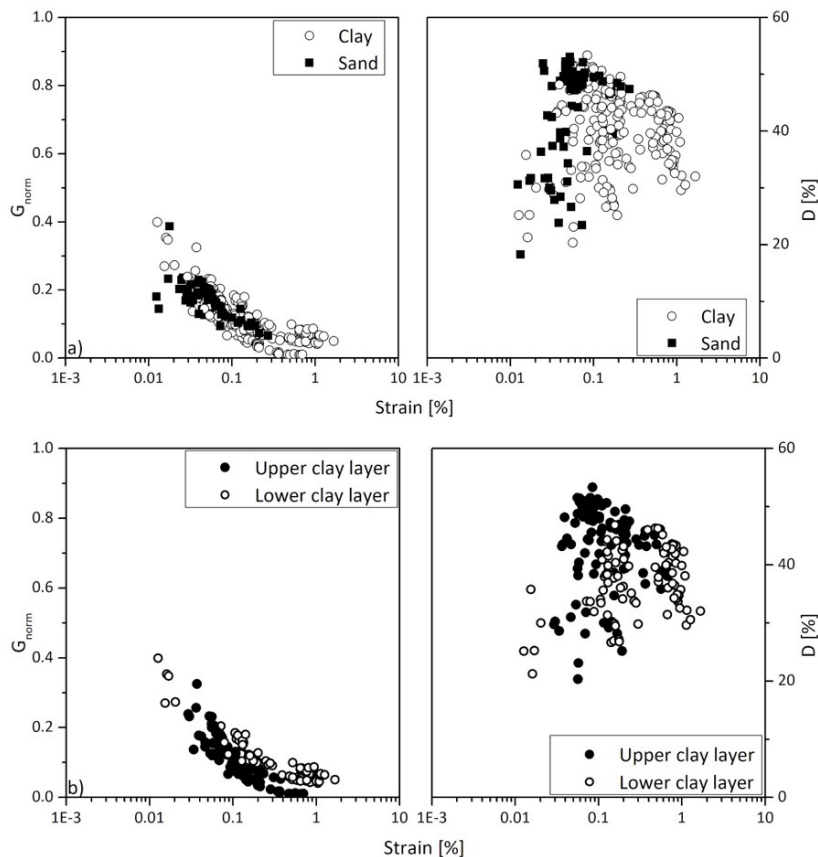


**Figure 10.** Normalized shear modulus and damping versus strain: (a) Difference between sand and clay data; (b) Difference of results between the upper and lower clay layers.

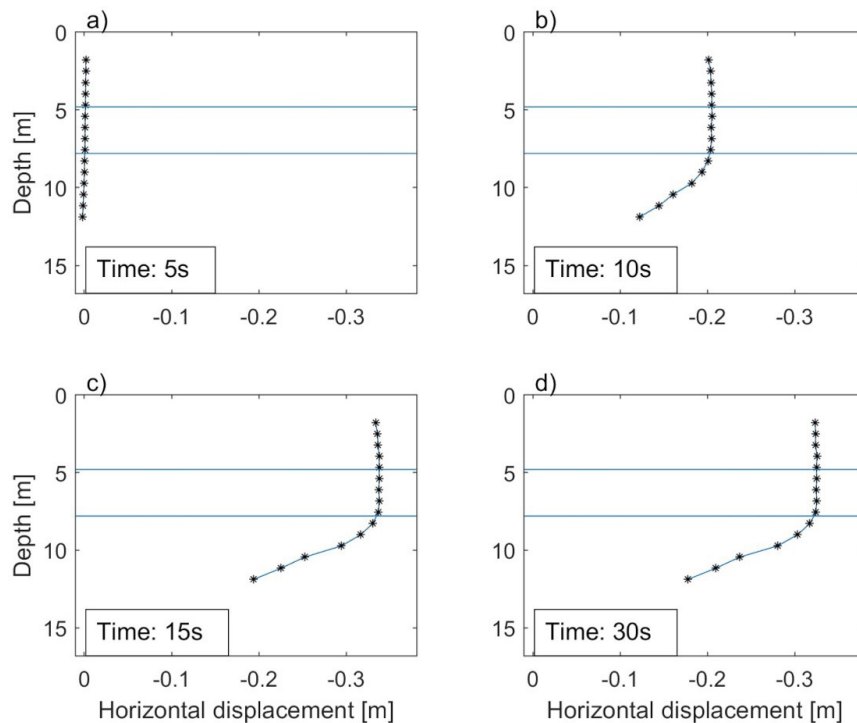


**Figure 11.** Horizontal displacement for EQ4 and all PIV markers, at different loading moments (prototype scale): (a) 5 s; (b) 10 s; (c) 15 s; (d) 30 s. Division between layers marked with a blue line.

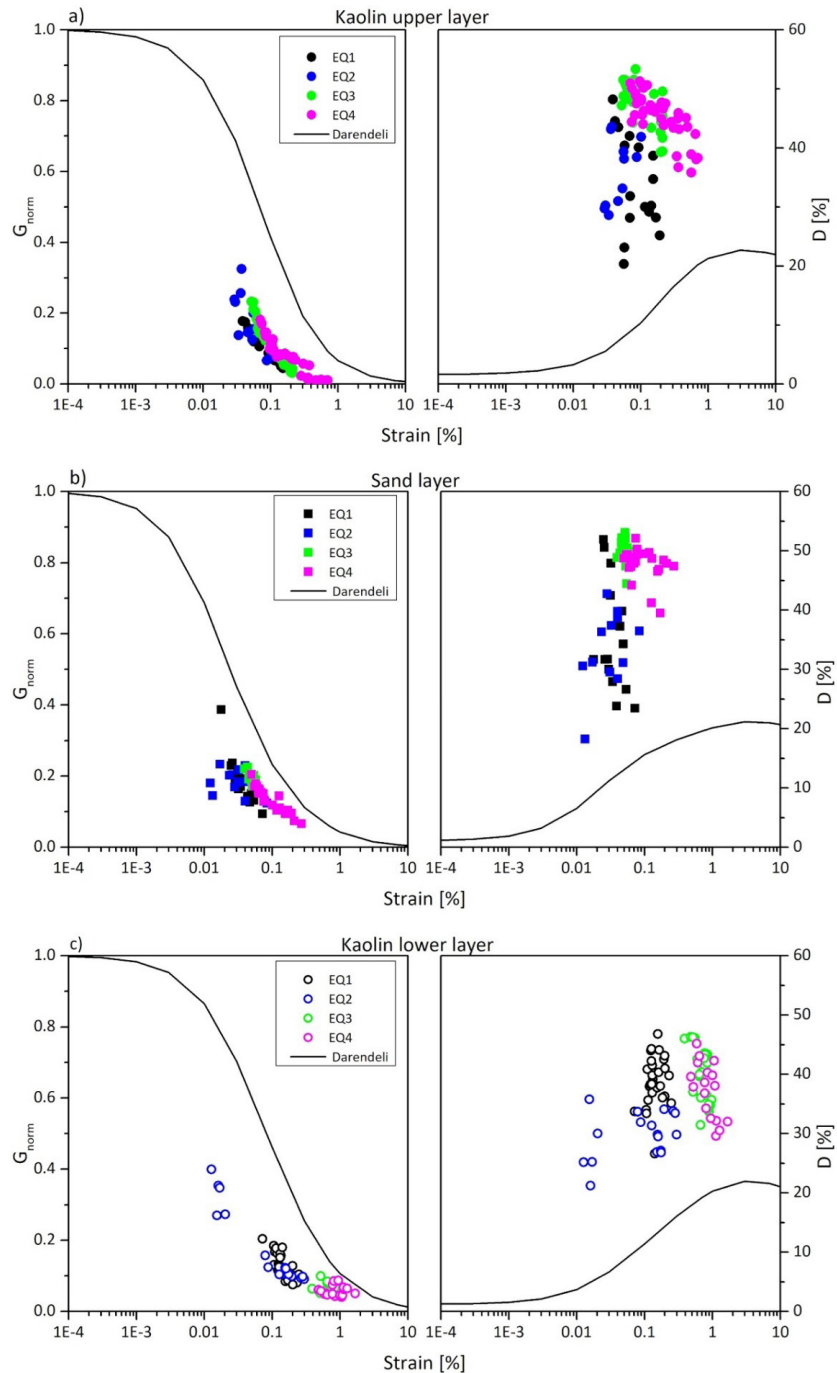


**Figure 12.** Shear modulus degradation and damping variation: (a) Clay upper layer; (b) Sand layer; (c) Clay lower layer.

calculations increases leading to values larger than the reference ones. It is important to note that the reference curves (Darendeli, 2001) were based on a different type of test with some unrelated conditions.

### 3.3.3 Strain rate effect

Multiple authors observed a correlation between the dynamic response of soil with the strain rate ( $\dot{\gamma}$ ) generated

during each log cycle. Sheahan et al. (1996) summarize numerous percent changes in  $s_u$  per log cycle, varying between 0% - 17%. Quinn et al. (2012) performed a series of triaxial tests on kaolin samples, at strain rates from 1%/h to 180,000%/h. They found that the rate effects not only change with the log cycle with a specific fractional increase, in reality, follows a backbone curve. It was also pointed out that soil type influences strain rate effects.

Due to its single frequency nature, sinusoidal signals are simple and predictable. Further calculations were limited for this load. A relation between the strain rate compatible shear strength ( $(s_u)_d$ ) and undrained shear strength ( $s_u$ ) was calculated for each trio of markers using Equation 5 (Afacan et al., 2014).

$$\frac{(s_u)_d}{s_u} = (1 + \lambda)^{\log_{10}\left(\frac{\dot{\gamma}}{\dot{\gamma}_{ref}}\right)} \quad (5)$$

where:

- $(s_u)_d$  – Strain rate compatible shear strength [kPa]
- $s_u$  – Undrained shear strength [kPa]
- $\lambda$  – Fractional increase of normalized shear strength per log cycle
- $\dot{\gamma}$  – Strain rate [%/s]

$\dot{\gamma}_{ref}$  – Reference strain rate [%/s]

For each input, the average strain rate ( $\dot{\gamma}_{average}$ ) was calculated by dividing the accumulated strain by the input duration (model scale). The fractional increase per log cycle ( $\lambda = 0.09$ ) was obtained from Sheahan et al. (1996), and the reference strain rate ( $\dot{\gamma}_{ref} = 0.006\%/s$ ) was taken from Afacan et al. (2014). Figure 13a shows the shear strength profile obtained from CPT, as well as the strain rate compatible shear strength. Larger values were observed at greater depths, where larger deformations occurred. This adjustment increased soil resistance by 12% to 41% compared to the CPT value. Figures 13b and 13c display the backbone stress strains curve (Darendeli, 2001) and the normalized shear stress versus the average shear strain ( $\gamma_a$ ) for each loop. In Figure 13b, the cyclic shear strength ( $\tau_{f,cy}$ , Equation 6) normalized with  $s_u$ , reached values above unity, whereas in Figure 13c, cyclic shear strength

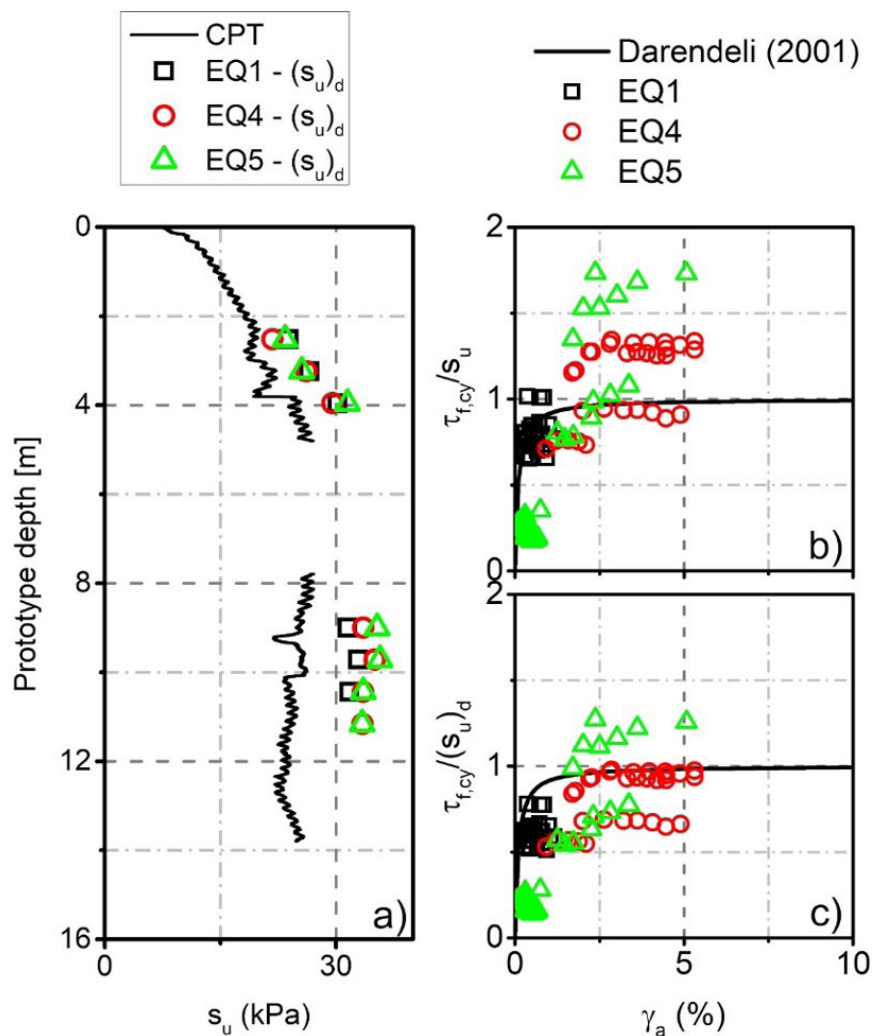


**Figure 13.** Strain rate effect. (a) Measured undrained shear strength and strain rate compatible shear strength profile; (b) Normalized cyclic shear stress by the measured undrained shear strength; (c) Normalized cyclic shear stress by the strain rate compatible shear strength. Model scale.

normalized with the strain rate compatible shear strength ( $\tau_{f,cy} / (s_u)_d$ ) exhibited points around unity. This statement highlights the importance of applying strain-rate corrections to shear strengths for site-response problems. It is observed that strain rates mobilized in centrifuge models are higher than those expected for prototype conditions.

$$\tau_{f,cy} = \tau_s + \tau_{cy} \quad (6)$$

$\tau_{f,cy}$  – Cyclic shear strength [kPa]

$\tau_s$  – Static shear stress [kPa]

$\tau_{cy}$  – Cyclic shear stress [kPa]

The normalized shear modulus ( $G_{norm}$ ), explained previously, is used for evaluating the dynamic behavior of soil and has been used to evaluate degradation curves in numerical modeling programs such as DEEPSOIL (Hashash et al., 2016) and OpenSEES (McKenna et al., 2010) for nonlinear analyses. Undrained shear strength is also important for the calibration of numerical models. To match the undrained shear strength of clay layers, a strain rate correction factor must be applied to reflect the larger shear stresses that can be mobilized during seismic shaking. This effect is more pronounced in centrifuge testing, where there is no compatibility between strain rates at the model and the prototype. Figure 13 demonstrates the importance of considering strain rate effects for calibrating numerical models, where strain rate corrected values of shear stress were compatible with the expected values.

As discussed earlier, the calculation of average strain rate ( $\dot{\gamma}_{average}$ ) involves dividing the accumulated strain by the input duration. This parameter is summarized in Figure 14a by the inclination of the dotted line. However, a more detailed analysis was performed by calculating the strain rate for each loop ( $\dot{\gamma}_{loop}$ ), which is defined as the inclination of the line that passes through the maximum and minimum values of time and shear strain for each loop, as shown in Figure 14b. Notably, for the sinusoidal input, the average inclination of each loop differs from the overall average, indicating that

the strain rate varies throughout the test. This information is essential for understanding the dynamic behavior of the material under different loading conditions and for developing accurate numerical models to simulate this behavior.

Figure 15 presents the strain rate compatible normalized shear stress versus strain rate for each distinct strain stress loop ( $\dot{\gamma}_{loop}$ ) obtained from Figure 9, at different depths. Despite the sinusoidal inputs at different depths yielding strain rates of up to 60.6%/s in Equation 5, the strain rates calculated for each loop exceeded 100%/s, suggesting that  $\dot{\gamma}$  may have been underestimated. The normalized shear stress increase with strain rate until stabilizing. This behavior is in line with the backbone curve described by Quinn et al. (2012).

Figure 16 compares the normalized shear stress calculated using the average strain rate ( $\dot{\gamma}_{average}$ ) with the strain rate evaluated for each strain-stress loop ( $\dot{\gamma}_{loop}$ ), color-coded based on  $\dot{\gamma}_{loop}$ . On average, the values of strain rate compatible undrained strength, adjusted for each load/unload loop were higher than those calculated using  $\dot{\gamma}_{average}$ . The difference between the two methods was more pronounced at higher shear stress values due to the increase in strain rate for each loop with shear stress. In Figure 16, it is presented all points below 50%/s (blue) yielded normalized shear stress values below 0.8, whereas all data points above 100%/s (orange) had  $\tau_{f,cy} / (s_u)_d$  above 0.9.

Table 3 presents the maximum values of the average strain rate ( $\dot{\gamma}_{average}$ ) for each input used to calculate  $(s_u)_d$ , the maximum strain rate calculated for each loop, the corresponding values of normalized shear strength, and the percentile increase. Shear strain rates calculated using accumulated strain and input duration can underestimate soil solicitation during dynamic motion, as show in Figure 16. However, for the strain rate range studied, the increase resulting from using the strain rate calculated for each loop is negligible, amounting to a maximum increase of 5.8%. Higher strain rates may result in a greater difference between the normalized rates and justify calculating the strain rate for each loop.

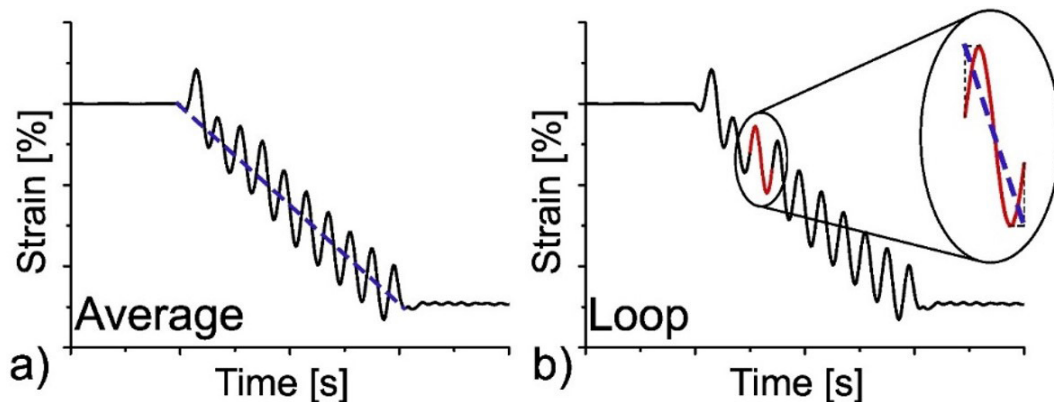


**Figure 14.** Time history shear strain, strain rate calculation. (a) Strain rate calculated by the average; (b) Strain rate calculated for each loop.

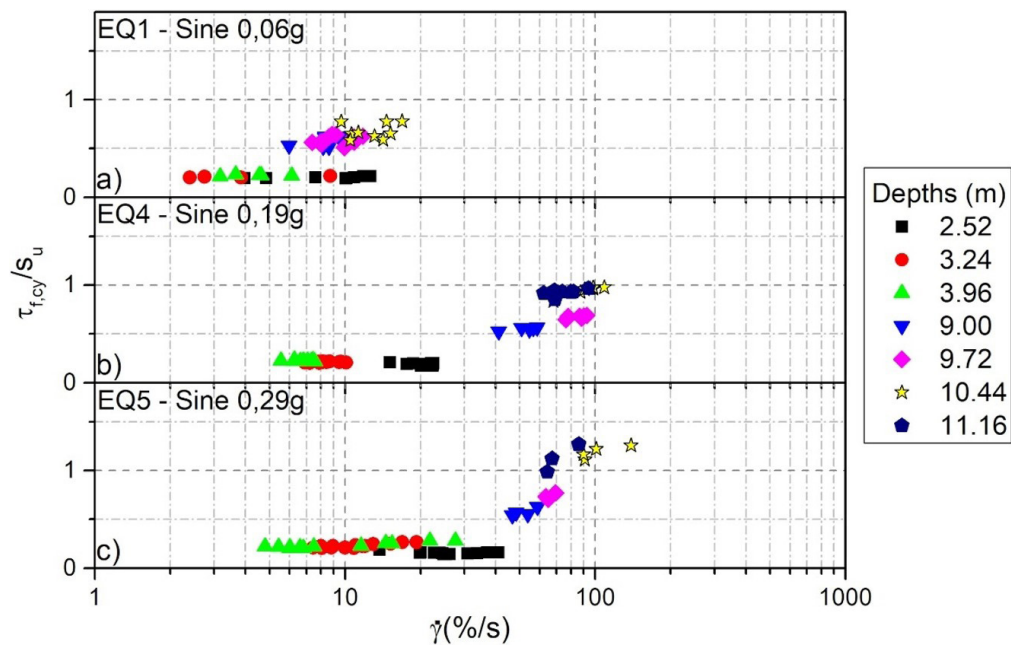


Figure 15. Strain rate compatible normalized shear stress versus strain rate. Model scale.

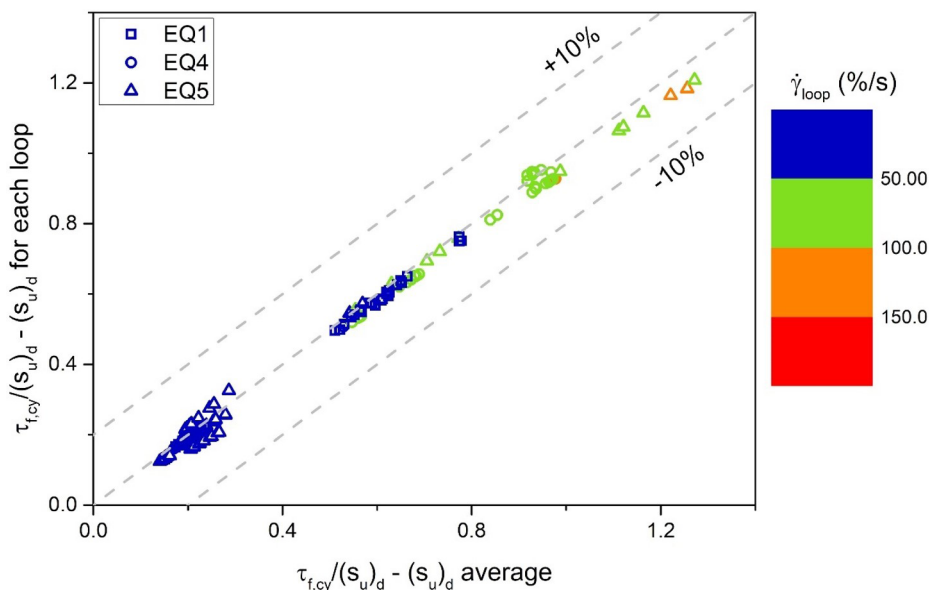


Figure 16. Strain rate compatible normalized shear stress versus strain rate.

Table 3. Shear strain rate, average and for each loop.

	$\dot{\gamma}_{average} \text{ (%/s)}$	$\frac{(s_u)_d, average}{s_u}$	$\dot{\gamma}_{loop} \text{ (%/s)}$	$\frac{(s_u)_d, loop}{s_u}$	$\frac{(s_u)_d, loop}{(s_u)_d, average} \text{ (%)}$
EQ1	7.0	1.30	16.9	1.35	3.8
EQ4	29.5	1.37	108.6	1.45	5.8
EQ5	60.6	1.41	139.2	1.46	3.5

## 4. Conclusions

In this study, Particle Image Velocimetry (PIV) analysis was used to evaluate the results of a centrifuge test of a gentle slope consisting of a sand layer sandwiched between two clay layers. The PIV analysis was validated by comparing it with data from accelerometers and LVDTs, yielding good agreement. By accurately measuring lateral displacements of soil profiles, PIV enables the evaluation of dynamic soil parameters in physical modelling while accounting for shear strain accumulation.

The shear stress versus shear strain graph revealed an accumulation of strains during loading, consistent with previous findings in the literature (Biscontin & Pestana, 2006). A decline in the shear modulus ( $G$ ) and increase in damping were also observed.

The results showed lower values of modulus degradation than those reported in the literature for clay and sand. This behavior may be due to the increased reduction in the normalized shear modulus ( $G_{norm}$ ) resulting from the action of the static shear stress generated by the slope. Further investigation could be conducted to adjust a new set of modulus degradation curves to account for the slope angle.

Each of the three soil layers in the study displayed distinct behavior. The sand layer showed lower strain due to its higher resistance to strength degradation. On the other hand, the upper clay layer had lower normalized shear modulus values compared to the deeper layer. This can be attributed to the increase in static shear stress with depth. The lower layers exhibited more pronounced shear modulus degradation curves, which could potentially be corrected for slope angle effects.

Strain rate analysis for the clay layers supported previous findings in the literature (Afacan et al., 2014; Quinn et al., 2012). Undrained shear strength was found to increase with strain rate and should be accounted for in dynamic tests, particularly in centrifuge tests where the model/scale factor for strain rate depends on the centrifuge acceleration. Although the strain rate calculated for each loop yielded higher than  $\dot{\gamma}_{average}$ , this increase was insignificant and did not justify the refinement. However, higher shear stress could generate sufficient strain rates that to sustain such analysis.

## Acknowledgements

The authors express their gratitude to the staff of the Schofield Centre at the University of Cambridge for conducting the testing program presented in this study. This research work is part of a collaborative effort between PETROBRAS and the Federal University of Rio de Janeiro, under a Cooperation Agreement aimed at investigating 'Seismic Centrifuge Modelling of Gentle Slopes' (Contractual Instrument 2017/00259-5). This project has also received partial funding from the Rio de Janeiro State Research

Foundation (FAPERJ) and the National Institute of Science and Technology – REAGEO

## Declaration of interest

The authors have no conflicts of interest to declare. All co-authors have observed and affirmed the contents of the paper and there is no financial interest to report.

## Authors' contributions

Lucas Chinem Takayassu: formal analysis, software, visualization, writing – original draft. Cristian Yair Soriano Camelo: conceptualization, data curation, methodology, writing – original draft. Marcio de Souza Soares de Almeida: conceptualization, project administration, writing – review & editing. Maria Cascão Ferreira de Almeida: conceptualization, project administration, writing – review & editing. Santana Phani Gopal Madabhushi: data curation, methodology, writing – review & editing. Ricardo Garske Borges: supervision, review & editing.

## Data availability

The datasets generated analyzed in the course of the current study are available from the corresponding author upon request.

## List of symbols

$e$	Void ratio
$e_{max}$	Maximum void ratio
$e_{min}$	Minimum void ratio
$g$	Gravity
$k$	Fitting function (Hardin & Black, 1969)
$m$	Fitting function (Hardin & Black, 1969)
$n$	Plastic volumetric strain ratio
$p'$	Average effective stress
$p_r$	Reference stress
$q_c$	Measured tip resistance
$s_u$	Undrained shear strength
$(s_u)_d$	Strain rate compatible shear strength
$(s_u)_{d, average}$	Strain rate compatible shear strength, calculated with $\dot{\gamma}_{average}$
$u$	Horizontal displacement
$\ddot{u}$	Horizontal acceleration
$v_s$	Shear wave velocity
$w$	Water content
$z$	Depth
$A$	Fitting function (Hardin & Black, 1969)
CPT	Cone Penetration Test
$D_{595}$	Significant Durations
$F(e)$	Fitting function
$G_0$	Initial shear modulus

$G_{\text{norm}}$	Normalized shear modulus
$G_s$	Specific Gravity
$G_{\text{sec}}$	Secant shear modulus
$K$	Normally consolidated strength ratio
$LL$	Liquid Limit
LVDT	Linearly Varying Differential Transformers
$N_{\text{kt}}$	Cone factor
OCR	Overconsolidation ratio
PGA	Peak Ground Accelerations
$PI$	Plasticity Index
PIV	Particle Image Velocimetry
$PL$	Plastic Limit
RCTS	Resonant Column Torsional Shear
RD	Relative density
$\alpha$	Slope angle
$\gamma$	Shear strains
$\dot{\gamma}$	Strain rate
$\dot{\gamma}_{\text{average}}$	Average reference strain rate
$\dot{\gamma}_{\text{loop}}$	Reference strain rate, calculated for each loop
$\dot{\gamma}_{\text{ref}}$	Reference strain rate
$\lambda$	Fractional increase of normalized shear strength per log cycle
$\rho$	Soil density
$\sigma'_v$	Effective vertical stress
$\tau$	Shear stress
$\tau_{\text{cy}}$	Cyclic shear stress
$\tau_{\text{f,cy}}$	Cyclic shear strength
$\tau_s$	Static shear stress
$\phi_{\text{crit}}$	Critical state friction angle

## References

- Afacan, K.B., Brandenberg, S.J., & Stewart, J.P. (2014). Centrifuge modeling studies of site response in soft clay over wide strain range. *Journal of Geotechnical and Geoenvironmental Engineering*, 140(2), 04013003. [http://dx.doi.org/10.1061/\(ASCE\)GT.1943-5606.0001014](http://dx.doi.org/10.1061/(ASCE)GT.1943-5606.0001014).
- Almeida, M.S.S. (1984). *Stage constructed embankments on soft clay* [Doctoral thesis]. Churchill College.
- Azeiteiro, R.J.N., Coelho, P.A.L.F., Taborda, D.M.G., & Grazina, J.C.D. (2017). Critical state–based interpretation of the monotonic behavior of hostun sand. *Journal of Geotechnical and Geoenvironmental Engineering*, 143(5), 04017004. [http://dx.doi.org/10.1061/\(ASCE\)GT.1943-5606.0001659](http://dx.doi.org/10.1061/(ASCE)GT.1943-5606.0001659).
- Biscontin, G., & Pestana, J.M. (2006). Factors affecting seismic response of submarine slopes. *Natural Hazards and Earth System Sciences*, 6(1), 97-107. <http://dx.doi.org/10.5194/nhess-6-97-2006>.
- Brennan, A.J., Thusyanthan, N.I., & Madabhushi, S.P. (2005). Evaluation of shear modulus and damping in dynamic centrifuge tests. *Journal of Geotechnical and Geoenvironmental Engineering*, 131(12), 1488-1497. [http://dx.doi.org/10.1061/\(ASCE\)1090-0241\(2005\)131:12\(1488\)](http://dx.doi.org/10.1061/(ASCE)1090-0241(2005)131:12(1488)).
- Chang, C.Y., Power, M.S., Tang, Y.K., & Mok, C.M. (1989). Evidence of nonlinear soil response during a moderate earthquake. In *Proc. 12th Int. Conf. on Soil Mechanics and Foundation Engineering*, Rio de Janeiro, Brazil, Vol. 3. Retrieved in April 5, 2023, from [https://www.issmg.org/uploads/publications/1/33/1989\\_03\\_0105.pdf](https://www.issmg.org/uploads/publications/1/33/1989_03_0105.pdf)
- Chian, S.C., Tokimatsu, K., & Madabhushi, S.P.G. (2014). Soil liquefaction–induced uplift of underground structures: physical and numerical modeling. *Journal of Geotechnical and Geoenvironmental Engineering*, 140(10), 04014057. [http://dx.doi.org/10.1061/\(ASCE\)GT.1943-5606.0001159](http://dx.doi.org/10.1061/(ASCE)GT.1943-5606.0001159).
- Colliat, J.L., Desrues, J., & Flavigny, F. (1986). Avantages et inconvénients de l'utilisation d'un système d'antifretage dans l'essai triaxial de compression. *Revue Française de Géotechnique*, 34, 41-55. <http://dx.doi.org/10.1051/geotech/1986034041>.
- Darendeli, M.B. (2001). *Development of a new family of normalized modulus reduction and material damping curves* [Doctoral thesis]. University of Texas.
- Elgamal, A., Yang, Z., & Parra, E. (2002). Computational modeling of cyclic mobility and post-liquefaction site response. *Soil Dynamics and Earthquake Engineering*, 22(4), 259-271. [http://dx.doi.org/10.1016/S0267-7261\(02\)00022-2](http://dx.doi.org/10.1016/S0267-7261(02)00022-2).
- Elgamal, A., Zeghal, M., Taboada, V., & Dobry, R. (1996). Analysis of site liquefaction and lateral spreading using centrifuge testing records. *Soil and Foundation*, 36(2), 111-121. [http://dx.doi.org/10.3208/sandf.36.2\\_111](http://dx.doi.org/10.3208/sandf.36.2_111).
- Ghosh, B., & Madabhushi, S.P.G. (2002). An efficient tool for measuring shear wave velocity in the centrifuge. In *Proceedings of the International Conference on Physical Modeling in Geotechnics: ICPMG'02* (pp. 119-124). St. John's, New Foundland, Canada: CRC Press / Balkema.
- Groholski, D.R., Hashash, Y.M.A., Kim, B., Musgrove, M., Harmon, J., & Stewart, J.P. (2016). Simplified model for small-strain nonlinearity and strength in 1D seismic site response analysis. *Journal of Geotechnical and Geoenvironmental Engineering*, 142(9), 04016042. [http://dx.doi.org/10.1061/\(ASCE\)GT.1943-5606.0001496](http://dx.doi.org/10.1061/(ASCE)GT.1943-5606.0001496).
- Hardin, B.O., & Black, W.L. (1969). Closure to “Vibration Modulus of Normally Consolidated Clay”. *Journal of the Soil Mechanics and Foundations Division*, 95(6), 1531-1537. <http://dx.doi.org/10.1061/JSFEAQ.0001364>.
- Hashash, Y.M.A., Musgrove, M.I., Harmon, J.A., Groholski, D.R., Phillips, C.A., & Park, D. (2016). *DEEPSOIL 6.1: User Manual*. Deepsoil.
- Herrerros, J.P. (2020). *Dynamic soil-structure interaction of pile foundations: experimental and numerical study* [Doctoral thesis]. École centrale de Nantes.
- Hess, R. (2010). *Blender foundations: the essential guide to learning Blender 2.6*. Focal Press/Elsevier.
- Hoque, E., & Tatsuoka, F. (2000). *Kinematic elasticity of a granular material*. In *Paper presented at the ISRM International Symposium*, Melbourne, Australia. Retrieved in April 5, 2023, from <https://onepetro.org/>

- ISRMIS/proceedings-abstract/IS00/All-IS00/ISRM-IS-2000-231/50956.
- Kokusho, T. (1980). Cyclic triaxial test of dynamic soil properties for wide strain range. *Soil and Foundation*, 20(2), 45-60. [http://dx.doi.org/10.3208/sandf1972.20.2\\_45](http://dx.doi.org/10.3208/sandf1972.20.2_45).
- Kramer, S.L. (1996). *Geotechnical earthquake engineering*. Prentice Hall.
- Lau, B.H. (2015). *Cyclic behaviour of monopile foundations for offshore wind turbines in clay* [Doctoral thesis]. University of Cambridge.
- Li, Z., Escoffier, S., & Kotronis, P. (2013). Using centrifuge tests data to identify the dynamic soil properties: application to Fontainebleau sand. *Soil Dynamics and Earthquake Engineering*, 52, 77-87. <http://dx.doi.org/10.1016/j.soildyn.2013.05.004>.
- Lu, C.-C., & Hwang, J.-H. (2019). Nonlinear collapse simulation of Daikai Subway in the 1995 Kobe earthquake: necessity of dynamic analysis for a shallow tunnel. *Tunnelling and Underground Space Technology*, 87, 78-90. <http://dx.doi.org/10.1016/j.tust.2019.02.007>.
- Madabhushi, G. (2014). *Centrifuge modelling for civil engineers*. CRC Press/Taylor & Francis.
- Madabhushi, G.S.P., Haigh, S.K., Houghton, N.E., & Gould, E. (2012). Development of a servo-hydraulic earthquake actuator for the Cambridge Turner beam centrifuge. *International Journal of Physical Modelling in Geotechnics*, 12(2), 77-88. <http://dx.doi.org/10.1680/ijpmg.11.00013>.
- Masson, D. G., Harbitz, C. B., Wynn, R. B., Pedersen, G., & Løvholt, F. (2006). Submarine landslides: processes, triggers and hazard prediction. *Philosophical Transactions of the Royal Society A: Mathematical, Physical and Engineering Sciences*, 364(1845), 2009-2039. <https://doi.org/10.1098/rsta.2006.1810>
- McKenna, F., Scott, M.H., & Fenves, G.L. (2010). Nonlinear Finite-Element Analysis Software Architecture Using Object Composition. *Journal of Computing in Civil Engineering*, 24(1), 95-107. [http://dx.doi.org/10.1061/\(ASCE\)CP.1943-5487.0000002](http://dx.doi.org/10.1061/(ASCE)CP.1943-5487.0000002).
- Quinn, T.A.C., Robinson, S., & Brow, M.J. (2012). *High strain rate characterisation of kaolin and its application to rapid load pile testing*. In *Proc. Kanazawa. 9th Int. Conf. on Testing & Design Methods for Deep Foundations*, Kanazawa. Retrieved in April 5, 2023, from [https://www.researchgate.net/publication/304282658\\_High\\_strain\\_rate\\_characterisation\\_of\\_kaolin\\_and\\_its\\_application\\_to\\_rapid\\_load\\_pile\\_testing](https://www.researchgate.net/publication/304282658_High_strain_rate_characterisation_of_kaolin_and_its_application_to_rapid_load_pile_testing).
- Rayhani, M.H.T., & El Naggari, M.H. (2007). Centrifuge modeling of seismic response of layered soft clay. *Bulletin of Earthquake Engineering*, 5(4), 571-589. <http://dx.doi.org/10.1007/s10518-007-9047-0>.
- Sahoo, P.P., & Shukla, S.K. (2021). Time-history analysis of soil slope subjected to seismic loadings. *Soil Mechanics and Foundation Engineering*, 58(2), 130-137. <http://dx.doi.org/10.1007/s11204-021-09717-z>.
- Sathialingam, N., & Kutter, B. L. (1989). *The effects of high strain rate and high frequency loading on soil behavior in centrifuge model tests (NCEL Contract Report)*. California Univ Davis, from: <https://apps.dtic.mil/sti/citations/ADA212089>.
- Schofield, A.N. (1980). Cambridge geotechnical centrifuge operations. *Geotechnique*, 30(3), 227-268. <http://dx.doi.org/10.1680/geot.1980.30.3.227>.
- Sheahan, T.C., Ladd, C.C., & Germaine, J.T. (1996). Rate-dependent undrained shear behavior of saturated clay. *Journal of Geotechnical Engineering*, 122(2), 99-108. [http://dx.doi.org/10.1061/\(ASCE\)0733-9410\(1996\)122:2\(99\)](http://dx.doi.org/10.1061/(ASCE)0733-9410(1996)122:2(99)).
- Soriano Camelo, C.Y., Almeida, M.C.F., & Almeida, M. (2022). Centrifuge modeling of the seismic behavior of soft clay slopes. *Journal of Geotechnical and Geoenvironmental Engineering*, 148(11), 04022089. [http://dx.doi.org/10.1061/\(ASCE\)GT.1943-5606.0002884](http://dx.doi.org/10.1061/(ASCE)GT.1943-5606.0002884).
- Soriano Camelo, C.Y., Almeida, M.C.F., Madabhushi, S.P.G., Stanier, S.A., & Almeida, M. (2021). Seismic centrifuge modeling of a gentle slope of layered clay, including a weak layer. *Geotechnical Testing Journal*, 45(1), 20200236. <http://dx.doi.org/10.1520/GTJ20200236>.
- Tarazona, S.F.M., Almeida, M.C.F., Bretschneider, A., Almeida, M.S.S., Escoffier, S., & Garske, R.B. (2019). Evaluation of seismic site response of submarine clay canyons using centrifuge modelling. *International Journal of Physical Modelling in Geotechnics*, 172, 1-38.
- Tsai, C.-C., & Hashash, Y.M. (2009). Learning of dynamic soil behavior from downhole arrays. *Journal of Geotechnical and Geoenvironmental Engineering*, 135(6), 745-757. [http://dx.doi.org/10.1061/\(ASCE\)GT.1943-5606.0000050](http://dx.doi.org/10.1061/(ASCE)GT.1943-5606.0000050).
- Vardanega, P.J., Lau, B.H., Lam, S.Y., Haigh, S.K., Madabhushi, S.P.G., & Bolton, M.D. (2012). Laboratory measurement of strength mobilisation in kaolin: link to stress history. *Géotechnique Letters*, 2(1), 9-15. <http://dx.doi.org/10.1680/geolett.12.00003>.
- Viggiani, G., & Atkinson, J.H. (1995). Stiffness of fine-grained soil at very small strains. *Geotechnique*, 45(2), 249-265. <http://dx.doi.org/10.1680/geot.1995.45.2.249>.
- Vucetic, M., & Dobry, R. (1991). Effect of soil plasticity on cyclic response. *Journal of Geotechnical Engineering*, 117(1), 89-107. [http://dx.doi.org/10.1061/\(ASCE\)0733-9410\(1991\)117:1\(89\)](http://dx.doi.org/10.1061/(ASCE)0733-9410(1991)117:1(89)).
- Vucetic, M., & Mortezaie, A. (2015). Cyclic secant shear modulus versus pore water pressure in sands at small cyclic strains. *Soil Dynamics and Earthquake Engineering*, 70, 60-72. <http://dx.doi.org/10.1016/j.soildyn.2014.12.001>.
- Wroth, C.P. (1984). The interpretation of in situ soil tests. *Geotechnique*, 34(4), 449-489. <http://dx.doi.org/10.1680/geot.1984.34.4.449>.
- Yang, Z., Yuan, J., Liu, J., & Han, B. (2017). Shear modulus degradation curves of gravelly and clayey soils based on kik-net in situ seismic observations. *Journal of Geotechnical and Geoenvironmental Engineering*, 143(9), 06017008. [http://dx.doi.org/10.1061/\(ASCE\)GT.1943-5606.0001738](http://dx.doi.org/10.1061/(ASCE)GT.1943-5606.0001738).

- Zeghal, M., Elgamal, A.-W., Tang, H.T., & Stepp, J.C. (1995). Lotung downhole array. II: evaluation of soil nonlinear properties. *Journal of Geotechnical Engineering*, 121(4), 363-378. [http://dx.doi.org/10.1061/\(ASCE\)0733-9410\(1995\)121:4\(363\)](http://dx.doi.org/10.1061/(ASCE)0733-9410(1995)121:4(363)).
- Zhang, C., White, D., & Randolph, M. (2011). Centrifuge modeling of the cyclic lateral response of a rigid pile in soft clay. *Journal of Geotechnical and Geoenvironmental Engineering*, 137(7), 717-729. [http://dx.doi.org/10.1061/\(ASCE\)GT.1943-5606.0000482](http://dx.doi.org/10.1061/(ASCE)GT.1943-5606.0000482).